Application of High-Order Flux Reconstruction with Artificial Viscosity Shock Capturing to Heat Flux Prediction

Ray Vandenhoeck[1], Andrea Lani[2], Johan Steelant[3]

Abstract

Obtaining accurate heat flux predictions for high-speed flows remains challenging and typically requires excessively fine meshes. The present work applies the high-order finite element-type Flux Reconstruction (FR) method and a Localized Laplacian Artificial Viscosity (LLAV) method to two high-speed benchmark test cases. More specifically, the Mach 3 viscous flow over a flat plate with linearly varying wall temperature and the Mach 17.6 viscous flow over a cylinder with a constant wall temperature are considered. An accurate heat flux prediction for both test cases is obtained at different orders of accuracy up to 10-th order using coarse meshes. For the flat plate case, the obtained heat flux is compared with the analytical solution from the Chapman-Rubesin approach. For the cylinder case, the heat flux is compared with results from the literature. For both cases a good agreement is found. Finally, the influence of the shock capturing method and the characterizing parameters of the FR method, including the correction polynomials, point distributions and interface flux schemes, on the predicted heat flux of the cylinder case is investigated.

Keywords: *Hypersonics, High-Order CFD, Flux Reconstruction, Artificial Viscosity*

Nomenclature

Latin

c − LLAV scaling factor
Cp − Pressure coefficient
c_p − Heat capacity at constant pressure
d − Deviation
J − Jacobian
$_k\mathbf{F}_i$ − Flux vector in point k for variable i
h − Correction function
$\bar{h}$ − Characteristic element length
l_k − Lagrange polynomial related to point k
M − Mach number
N − Number of mesh elements
N_{dim} − Number of dimensions
N_{eq} − Number of equations
N_f − Number of flux points
N_s − Number of solution points
P − Polynomial order
p − Pressure
S − Smoothness

St − Stanton number
$_k\mathbf{q}_i$ − Corrected gradient vector in point k for variable i
q − Heat flux
T − Temperature
t − Time
$_k\mathbf{u}$ − Conservative state vector in point k
V − Velocity
$\mathbf{x}$ − Coordinate vector

Greek

ε − Artificial viscosity
Θ − Mapping function
κ − Spectrum parameter of artificial viscosity
λ − Eigenvalue
$\boldsymbol{\xi}$ − Coordinate vector in standard domain
ρ − Density
Ω − Computational domain

Superscripts

$\hat{}$ − Variable in standard domain

[1]*Department of Mechanical Engineering, KU Leuven, Leuven, Belgium; von Karman Institute for Fluid Dynamics, Sint-Genesius-Rode, Belgium; ray.vandenhoeck@kuleuven.be*

[2]*Centre for mathematical Plasma-Astrophysics, KU Leuven, Leuven, Belgium; von Karman Institute for Fluid Dynamics, Sint-Genesius-Rode, Belgium; andrea.lani@kuleuven.be*

[3]*Department of Mechanical Engineering, KU Leuven, Leuven, Belgium; ESA/ESTEC, Noordwijk, The Netherlands; Johan.Steelant@esa.int*

δ − Approximate polynomial
D − Discontinuous value
I − Interface value
Subscripts
∞ − Free stream value
0 − Reference value

AV − Artificial viscosity
C − Convection
D − Diffusion
t − Total value
w − Wall value

1. Introduction

In the design of the thermal protection system of hypersonic vehicles, assessing the heat flux experienced during the different flight phases is crucial. Traditionally, low-order Computational Fluid Dynamics (CFD) methods, such as second-order finite volume, are used for this purpose. However, these methods typically introduce a large numerical dissipation and require extremely fine meshes to obtain accurate heat flux predictions. Recently, compact Finite Element-type (FE) high-order methods have drawn considerable attention due to an increased computational efficiency over their low-order counterparts. High-order methods generally introduce less numerical dissipation and allow for the use of coarser meshes while obtaining the same or better accuracy. The Flux Reconstruction (FR) formulation in particular represents one of the most recent and promising family of schemes. However, one of the main pacing item for these types of methods is their lack of adequate shock capturing techniques. Consequently, only limited results with high-order FE-type methods have been obtained for super- or hypersonic flows [1].

The present paper applies the FR approach with an artificial viscosity shock capturing method to the supersonic viscous flow over a flat plate and the hypersonic viscous flow over a cylinder. It is demonstrated that the FR method obtains an accurate heat flux prediction for both cases. The FR method is presented in section 2. Section 3 describes the shock capturing method. The two cases are presented in section 4.

2. Flux Reconstruction

The FR method is a high-order Finite Element-type (FE) method that was originally developed by Huynh in [2]. The formulation of the FR approach proposed by Huynh is applicable to 1D advection problems and can be extended to quadrilateral and hexahedral (tensor) elements through tensor products of the one-dimensional base and correction functions. In [3, 4], the FR scheme was extended to advection-diffusion problems on both simplex and tensor elements. In this case, the flux also depends on the gradient of the solution, and the reconstruction procedure is applied to both the solution and the flux.

The FR solver used in the present work is implemented in the COOLFluiD[1] platform and is described in detail in [5, 6]. More information on the development of COOLFluiD as a whole can be found in [7, 8]. Since the present solver uses tensor elements, the FR procedure for tensor elements is outlined in this section.

2.1. FR for Tensor Elements

Consider solving a system of N_{eq} advection-diffusion conservation equations on an arbitrary domain Ω, given by its i-th equation:

$$\frac{\partial u_i(\mathbf{x}, t)}{\partial t} = -\nabla \cdot \mathbf{F}_i(\mathbf{u}, \nabla\mathbf{u}) \text{ for } i = \{1, \dots, N_{eq}\} \text{ and } \mathbf{x} \in \Omega. \tag{1}$$

In this equation, t represents the time variable, $\mathbf{x}$ contains the space dimensional variables, in 3D being $\mathbf{x} = (x, y, z)$, u_i is the i-th conservative variable for which the system is solved, and $\mathbf{F}_i$ is the flux vector related to the i-th conservative variable. The Navier-Stokes equations can be written as a system of conservation equations, equivalent to Eq. 1. The FR method is classified as an FE-type method. Hence, the spatial domain Ω is partitioned into a finite number N of non-overlapping, non-empty, open

---

[1]https://github.com/andrealani/COOLFluiD/wiki

sub-domains Ω_n'. The closed domain corresponding to the union of the open sub-domain Ω_n' and its boundary Γ_n is called an element and is denoted by $\Omega_n = \Omega_n' \cup \Gamma_n$ such that:

$$\bigcup_{n=1}^{N} \Omega_n = \Omega \quad \text{with} \quad \bigcap_{n=1}^{N} \Omega_n = \emptyset. \tag{2}$$

The exact solution vector $\mathbf{u}$ of the conservation law in Eq. 1 is approximated by a function $\mathbf{u}_n^\delta$ within each element Ω_n. This function $\mathbf{u}_n^\delta$ corresponds for each u_i to a polynomial of degree P within Ω_n and is identically zero on $\Omega \setminus \Omega_n$. These polynomials are allowed to be discontinuous across elements. $\mathbf{u}^\delta$ is constructed through summation of the elemental solutions $\mathbf{u}_n^\delta$. In the same manner, the exact flux $\mathbf{F}$ is approximated by a polynomial of degree $P + 1$ within each sub-domain Ω_n, denoted by $\mathbf{F}_n^\delta$. The overall approximate flux $\mathbf{F}^\delta$ in the entire domain Ω is given by the sum of the elemental approximate fluxes such that:

$$\mathbf{u}^\delta = \sum_{n=1}^{N} \mathbf{u}_n^\delta \quad \text{and} \quad \mathbf{F}^\delta = \sum_{n=1}^{N} \mathbf{F}_n^\delta. \tag{3}$$

Each element Ω_n together with the approximate solution $\mathbf{u}_n^\delta$ and flux $\mathbf{F}_n^\delta$ inside it, is transformed to a standard reference element Ω_S, which in 3D is given by: $\Omega_S = \{\boldsymbol{\xi} = (\xi, \eta, \zeta) \mid -1 \leq \xi, \eta, \zeta \leq 1\}$. In this manner, the computations for all elements are done in the same reference domain Ω_S. The transformation between Ω_n and Ω_S is carried out by means of a mapping function $\Theta_n(\boldsymbol{\xi})$. The solution $\mathbf{u}_n^\delta$ within each sub-domain Ω_n can be obtained by solving the transformed conservation equation within the reference element Ω_S:

$$\frac{\partial \hat{u}_i^\delta}{\partial t} = -\nabla_{\boldsymbol{\xi}} \cdot \hat{\mathbf{F}}_i^\delta \quad \text{with} \quad \boldsymbol{\xi} \in \Omega_S, \tag{4}$$

with the transformed physical quantities given by:

$$\hat{u}_i^\delta = \hat{u}_i^\delta(\boldsymbol{\xi}, t) = J_n u_i^\delta(\Theta_n(\boldsymbol{\xi}), t) \quad \text{and} \quad \hat{\mathbf{F}}_i^\delta = \hat{\mathbf{F}}_i^\delta(\boldsymbol{\xi}, t) = \mathbf{F}_i^\delta(\Theta_n(\boldsymbol{\xi}), t). \tag{5}$$

In Eq. 5, J_n represents the Jacobian of the mapping $\Theta_n(\boldsymbol{\xi})$. From here on out, equations will only be considered in the standard domain and will only operate on the approximate polynomials for solution and flux. As such, hats on $\mathbf{u}$ and $\mathbf{F}$ and the superscript δ will be omitted in the rest of the present paper to make the equations more readable.

The FR method for solving Eq. 4 within the reference element Ω_S consists of seven subsequent steps. In the first step, a specific form for the approximate solution u_i is defined. To this end, a set of $N_s = (P + 1)^{N_{dim}}$ distinct solution points are chosen where N_{dim} is the spatial dimensionality of the problem to be solved. The solution points typically have a Gauss-Legendre distribution. At these solution points the values of u_i are assumed to be known. Consequently, the approximate solution u_i is defined as a degree P polynomial of the following form:

$$u_i = \sum_{k=1}^{N_s} {}_k u_i \, l_k(\boldsymbol{\xi}), \tag{6}$$

where ${}_k u_i$ is the value of u_i at the k-th solution point, and $l_k(\boldsymbol{\xi})$ is the base function polynomial associated with the k-th solution point. For the FR method the base functions are Lagrange polynomials. It is however not necessary to construct a multivariate Lagrange basis for tensor elements since a product of one-dimensional Lagrange polynomials in each spatial direction can be taken as follows:

$$u_i = \sum_{k=1}^{N_s} {}_k u_i \, l_k(\boldsymbol{\xi}) = \sum_{k=1}^{N_s} {}_k u_i \, l_k^\xi(\xi) l_k^\eta(\eta) l_k^\zeta(\zeta), \tag{7}$$

where $l_k^\xi(\xi)$ represents a 1D Lagrange polynomial in the ξ direction related to the k-th solution point. More detailed information on this can be found in [2].

The second step consists of determining a common interface solution u_i^I at the boundaries of the standard element Ω_S. On each face of the element, $P+1$ flux points are defined with the same distribution as the solution points, where the flux points of two neighbouring elements coincide. In order to compute the interface value at the f-th flux point ${}_f u_i^I$, Eq. 6 is evaluated in the f-th solution point. ${}_f u_i^I$ can be computed using an interface scheme, such as the second approach of Bassi and Rebay (BR2) [9]. Fig. 1 illustrates the process of computing the common interface values in 1D.
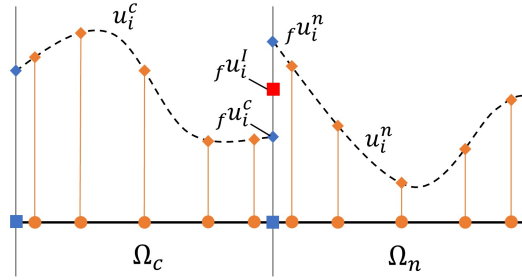
Fig 1. Computation of the common interface solutions; orange circles represent solution points and blue squares represent flux points

The third step of the FR method consists of calculating a corrected solution gradient ${}_k\mathbf{q}_i$ in each solution point k for each variable i. The previously defined interface solution values are used to obtain a continuous solution polynomial. To this end correction functions h_f for each flux point f are defined which have the following property for all flux points f and their opposite flux point g:

$$h_f(\boldsymbol{\xi}_f) = 1 \text{ and } h_f(\boldsymbol{\xi}_g) = 0. \tag{8}$$

Due to the tensor basis previously used for the solution points, these correction functions are one-dimensional and are only defined in the direction related to flux point f. Flux point g is on the same spatial direction as f but on the opposite side of the element as shown in Fig. 2. Furthermore from this figure it can be seen that to each solution point k there will be N_{dim} 1D Lagrange polynomials associated, each defined on a different spatial direction, shown by two dashed lines in Fig. 2. The form of the correction polynomials is defined by the VCJH scheme, which can be found in [10].
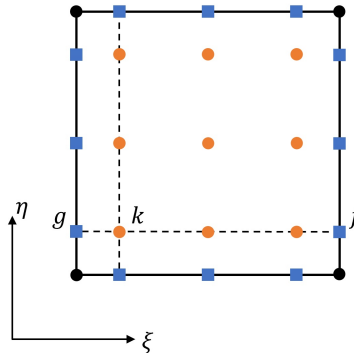

Fig 2. Illustration of tensor basis in 2D tensor element

The corrected solution gradient ${}_k\mathbf{q}_i$ is then computed via the following expression:

$$ {}_k\mathbf{q}_i = \nabla u_i + \sum_{f=1}^{N_f} \frac{dh_f}{d\xi^f}(\boldsymbol{\xi}_k)\left({}_f u_i^I - {}_f u_i\right)\mathbf{n}_f, \tag{9}$$

where N_f is the total number of flux points in an element, ξ^f the direction related to flux point f and $\mathbf{n}_f$ the normal vector in flux point f. Using Eq. 7 this can be written as:

$$_k q_i^d = \sum_{s=1}^{N_s} {}_s u_i \frac{dl_s^d}{d\xi}(\xi_k) + \sum_{f=1}^{N_f} \frac{dh_f}{d\xi^f}(\boldsymbol{\xi}_k) \left({}_f u_i^I - {}_f u_i \right) n_f^d, \tag{10}$$

where $_k q_i^d$ is the i-variable gradient in solution point k in the d-direction, where d is either ξ, η or ζ, and n_f^d d-component of the normal in flux point f.

The fourth step consists of calculating the approximate discontinuous flux polynomial $\mathbf{F}_i^D(\boldsymbol{\xi})$. To this end, the flux is computed at each solution point $\boldsymbol{\xi}_k$, denoted by $_k\mathbf{F}_i$. In general, the flux depends on the solution and the solution gradient. Consequently, the discontinuous flux is evaluated using the approximate solution $_k u_i$, and the corrected solution gradient $_k\mathbf{q}_i$. The approximate discontinuous flux $\mathbf{F}_i^D(\boldsymbol{\xi})$ is then constructed as a polynomial of degree P in the same manner as u_i in Eq. 7:

$$\mathbf{F}_i^D(\boldsymbol{\xi}) = \sum_{k=1}^{N_s} {}_k\mathbf{F}_i({}_k u_i, {}_k\mathbf{q}_i)\, l_k(\boldsymbol{\xi}) = \sum_{k=1}^{N_s} {}_k\mathbf{F}_i({}_k u_i, {}_k\mathbf{q}_i)\, l_k^\xi(\xi) l_k^\eta(\eta) l_k^\zeta(\zeta). \tag{11}$$

The fifth step of the FR framework involves computing the common interface fluxes $\mathbf{F}_i^I$ at the flux points. In order to compute these interface fluxes, it is necessary to first obtain in each flux point f the values of $_f u_i$ and $_f\mathbf{q}_i$ using Eq. 7 and 10. For the convective interface flux, an upwind biased approximate Riemann solver, like the Roe scheme [11], can be used. The diffusive interface flux is often calculated following the BR2 scheme [9].

The flux must be continuous across element boundaries in order to obtain a conservative scheme. Therefore, the sixth stage of the FR framework consists of adding a correction flux function $\mathbf{F}_i^C(\boldsymbol{\xi})$ to the approximate discontinuous flux $\mathbf{F}_i^D(\boldsymbol{\xi})$ resulting in the continuous flux $\mathbf{F}_i(\boldsymbol{\xi})$. The correction flux $\mathbf{F}_i^C$ is a polynomial of degree $P + 1$ defined in such a manner that the continuous flux $\mathbf{F}_i$ equals the common interface flux $\mathbf{F}_i^I$ in the flux points, while approximating the discontinuous flux $\mathbf{F}_i^D$ within the standard element. In order to satisfy the aforementioned requirements, $\mathbf{F}_i^C$ is constructed by means of the degree $P + 1$ correction functions $h_f(\xi)$ that were previously used to obtain the corrected gradient $_k\mathbf{q}_i$. Consequently, the correction flux function $\mathbf{F}_i^C(\boldsymbol{\xi})$ takes the following form:

$$\mathbf{F}_i^C(\boldsymbol{\xi}) = \sum_{f=1}^{N_f} h_f(\boldsymbol{\xi}) \left({}_f\mathbf{F}_i^I - {}_f\mathbf{F}_i^D \right), \tag{12}$$

where $_f\mathbf{F}_i^D = \mathbf{F}_i^D(\boldsymbol{\xi}_f)$. A schematic of the flux correction procedure within a 1D element with flux points f and g is given in Fig. 3.
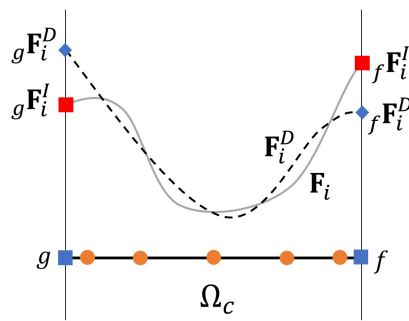

Fig 3. Correction procedure of the discontinuous flux such that the values of the total flux at the boundaries are equal to the interface value

The final step of the FR method consists of computing the divergence of the total flux $\mathbf{F}_i(\xi)$ at each solution point k. To this end the divergence of Eq. 11 and 12 is taken:

$$\nabla \cdot {}_k\mathbf{F}_i = \sum_{s=1}^{N_s} \sum_{d=1}^{N_{dim}} {}_sF_i^d \frac{dl_s^d}{d\xi^d}(\xi_k^d) + \sum_{f=1}^{N_f} \frac{dh_f}{d\xi^f}(\boldsymbol{\xi}_k) \left({}_f\mathbf{F}_i^I - {}_f\mathbf{F}_i^D \right) \cdot \mathbf{n}_f, \tag{13}$$

where ξ^d is the d-th spatial direction and ${}_sF_i^d$ the ξ^d-component of ${}_s\mathbf{F}_i$.

Finally, a time marching strategy such as the backward Euler method is applied to advance the approximate solution u_i in time using the following expression:

$$\frac{d_k u_i}{dt} = -\nabla \cdot {}_k\mathbf{F}_i. \tag{14}$$

3. Localized Laplacian Artificial Viscosity

Robust shock capturing is the main pacing item for high-order finite element-type CFD methods. In the vicinity of discontinuities within the flow field, spurious oscillations appear due to the Gibbs phenomenon. This effect is more severe for higher orders and for stronger shocks. The oscillations near the shock generally cause numerical instabilities and negative pressures or densities. The present paper uses a modified Localized Laplacian Artificial Viscosity (LLAV) scheme in order to alleviate oscillations caused by the Gibbs phenomenon as well as the harsh transient effects of hypersonics, as presented in [5].

The localized artificial viscosity method adds an artificial diffusive flux that depends on the local properties of the flow field in order to spread out the shock over one or more elements. In this way oscillations due to the Gibbs phenomenon around shocks are attenuated. Within the LLAV framework, the artificial viscosity is of a Laplacian type, as proposed in [12, 13]. The local artificial viscosity is only activated in areas of the flow field where discontinuities are present. To this end, a smoothness detector is used, of which several are proposed in [13].

LLAV shows better convergence characteristics compared to traditional limiters developed for FR, such as Multi-Dimensional Limiting Process (MLP) [14]. Furthermore, LLAV is readily adaptable to implicit time-marching schemes. However, LLAV cannot guarantee positivity of the solution for hypersonic test cases and requires fine-tuning of the maximum amount of artificial viscosity added, to work properly. Furthermore, the positivity preservation scheme presented in [5] is used to guarantee positivity. Below a concise overview of the used LLAV method is given.

Within the LLAV framework, an extra flux is added to the system of equations, such that:

$$\frac{d_k u_i}{dt} = -\nabla \cdot {}_k\mathbf{F}_{i,C} + \nabla \cdot {}_k\mathbf{F}_{i,D} + \nabla \cdot {}_k\mathbf{F}_{i,AV}, \tag{15}$$

where ${}_k\mathbf{F}_{i,C}$ is the convective flux, ${}_k\mathbf{F}_{i,D}$ the diffusive flux and ${}_k\mathbf{F}_{i,AV}$ the flux due to the artificial viscosity. ${}_k\mathbf{F}_{i,AV}$ is constructed as follows:

$$_k\mathbf{F}_{i,AV} = \varepsilon \nabla {}_k u_i, \tag{16}$$

where ε is the artificial viscosity. Within the FR framework, this means that the space discretisation procedure is also applied to a third flux. The gradients $\nabla_k u_i$ are approximated using the corrected solution gradients ${}_k\mathbf{q}_i$ as computed in Eq. 10. As such, the FR procedure, as described in section 2.1, is applied to:

$$_k\mathbf{F}_{i,AV} = \varepsilon {}_k\mathbf{q}_i. \tag{17}$$

The value of the artificial viscosity ε is computed in such a way that it is only active in discontinuous regions:

$$\varepsilon = \begin{cases} 0 & \text{if } S < S_0 - \kappa, \\ \frac{\varepsilon_0}{2}\left(1 + \sin\frac{\pi(S - S_0)}{2\kappa}\right) & \text{if } S_0 - \kappa \le S \le S_0 + \kappa, \\ \varepsilon_0 & \text{if } S > S_0 + \kappa, \end{cases} \tag{18}$$

where S is the smoothness in the current element, S_0 the reference smoothness, κ a parameter to control the working spectrum of the artificial viscosity and ε_0 the maximum artificial viscosity.

The smoothness for a P-th polynomial order FR method can be computed as follows, using the smoothness detector found in [12]:

$$S = \log_{10} \frac{\langle u_m - u_m^{P-1}, u_m - u_m^{P-1} \rangle}{\langle u_m, u_m \rangle}, \tag{19}$$

where u_m is the state variable that is monitored in order to detect discontinuities. For the Navier-Stokes equations, typically the density ρ or pressure p is used. When using the density ρ however, the smoothness detector can potentially detect the boundary layer as a shock since ρ can exhibit a strong gradient in the boundary layer. As such, unless mentioned otherwise, the pressure is used in the present work. u_m^{P-1} represents the monitored state variable projected on a $(P-1)$-th order polynomial. The operator $\langle \cdot , \cdot \rangle$ is the element-wise scalar product over the solution points. The reference smoothness is set equal to $S_0 = -5\log_{10} P - 0.5$, differing from the reference smoothness in [5]. In previous work, S_0 was set to $-3\log_{10} P$. It was found however that progressively reducing S_0 at higher orders significantly increases robustness, hence the factor of 3 is changed to 5. Furthermore, at P1 the theoretical maximum smoothness $S = 0$, which would be equal to the reference smoothness if $S_0 = -3\log_{10} P$. As such only half the smooth interval going from 0 to ε_0 would be utilized. As such, S_0 is reduced by 0.5 in order to utilize the full smooth interval at low orders, hence obtaining:

$$S_0 = -5\log_{10} P - 0.5. \tag{20}$$

The maximum artificial viscosity ε_0 is set to be:

$$\varepsilon_0 = f(P)\bar{h}|\lambda|_{max}, \tag{21}$$

where $\bar{h}$ is the characteristic length of the current element and $|\lambda|_{max}$ the maximum eigenvalue of the inviscid part of the system of equations. In order to take into account the order P of the FR method, following the approach of [13], $f(P)$ is set to:

$$f(P) = c(2 - \Delta\xi_{max}(P)), \tag{22}$$

where $\Delta\xi_{max}(P)$ is the sub-cell resolution, i.e. the largest distance between two solution points within the reference domain and c a constant. In order to avoid the need for fine-tuning the constant c, its value is calibrated following the procedure in [5].

4. Results

Two cases are considered: the supersonic viscous flow over a flat plate an the hypersonic viscous flow over a cylinder. The present section presents the results obtained for both cases, with an emphasis and the predicted heat flux.

4.1. Supersonic Viscous Flow over a Flat Plate

A supersonic viscous flow of air over a flat plate of 1m length is considered. The fluid is considered as an ideal gas and has the free stream conditions presented in Table 1.

Table 1. Free stream values for the supersonic flat plate case

M_∞	$p_\infty\ [Pa]$	$T_\infty\ [K]$
3	17106	500

The flat plate has a linearly varying temperature of the following form:

$$T_w = T_\infty \left(0.4 + 2.85\frac{x}{L} \right), \tag{23}$$

where L is the length of the flat plate, in this case $L = 1m$.

An analytical solution for this case is proposed by Chapman and Rubesin in [15]. The Chapman-Rubesin (CR) method is grounded in the laminar boundary layer theory and as such solves the flat plate boundary layer equations. The CR method assumes ideal gas behaviour and a constant Prandtl number and c_p. Furthermore, this approach is only valid when:

$$\frac{\partial T_w}{\partial x} \leq O\left(\frac{T_w - T_\infty}{\delta}\right),$$ (24)

where δ is a measure for the boundary layer thickness.

In [16] an assessment was made of the accuracy of the CR method. The CR solution is compared with the analytical shooting method presented by Anderson in [17] for a flat plate with an isothermal wall. A deviation of the heat flux predicted by CR with respect to the one predicted by the shooting method ranging from 0.2% to 10.8% is found for T_w/T_∞ ranging from 0.4 to 3.25. Consequently, the expected accuracy of the CR method is around 10%. To obtain the analytical CR solution of the present case, the code developed in [16] is used.

The used mesh is presented in Fig. 4. The flat plate is considered as a no-slip wall. On the horizontal boundary upstream of the flat plate a symmetry boundary condition is imposed. The left vertical and top horizontal boundaries are Dirichlet boundary conditions imposing the free stream values. On the right vertical boundary a supersonic outlet condition is imposed. In this way, due to the height of the domain, the shock induced by the boundary layer only touches the outlet boundary condition. The mesh contains 1792 quadrilateral element. 50 elements on the flat plate, 6 elements on the symmetry condition and 32 elements normal to the flat plate.
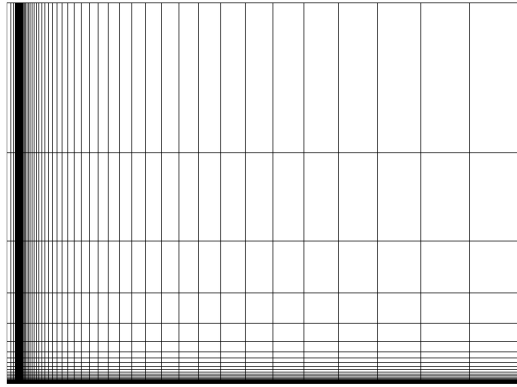

Fig 4. Mesh with 1792 quadrilateral elements used for the supersonic flat plate case

The FR method is used with a c_{SD} VCJH scheme [10] for the correction functions. The distribution of both the solution and flux points is the Gauss-Legendre distribution. For the convective interface fluxes, the AUSM$^+$ scheme is used, as proposed in [18, 19]. For the diffusive and artificial interface fluxes, the Local Approach scheme is used [20, 23]. For the LLAV scheme, κ is set to 0.5.

Fig. 5a presents the Stanton number for first up to fourth order of accuracy, i.e. polynomial orders $P0$ up to $P3$, comparing with the Stanton number obtained from the CR method. The Stanton number is defined as follows:

$$St = \frac{q_w}{c_p \rho_\infty V_\infty (T_{t,\infty} - T_w)},$$ (25)

where q_w is the wall heat flux and $T_{t,\infty}$ the total free stream temperature. Note that this definition is slightly different from the one used in [15, 16, 17] in order to be consistent with the Stanton number used in the case presented in section 4.2.

It is clear that at polynomial order P2 and P3 the FR method approaches the CR method closely, although not coinciding exactly and exhibiting some oscillation close to discontinuity of the leading edge. One remarkable feature of the Stanton number is the asymptote at approximately $x = 0.84m$. This is not due to an infinite heat flux, it is however due to the denominator of the Stanton number becoming zero when the wall temperature equals the total free stream temperature. This can easily be verified by considering the heat flux instead of the Stanton number, presented in Fig. 5b. For the heat flux there is no singularity and the FR solution once again approaches the CR solution. In order to estimate whether

(a) Stanton number   (b) Heat flux
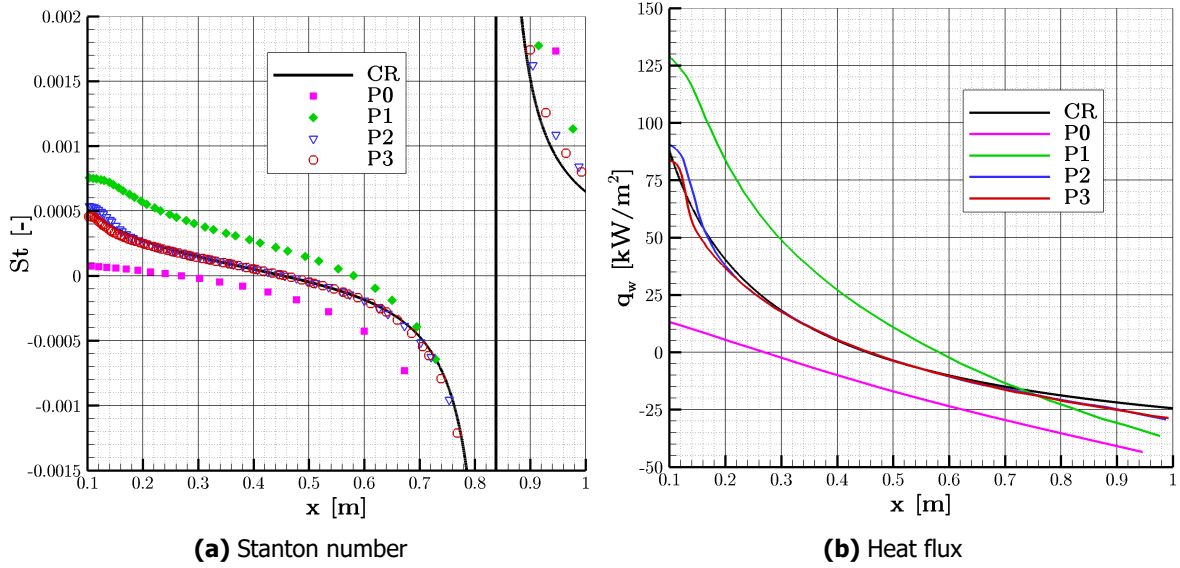
Fig 5. Supersonic flat plate P0 to P3 solutions

the deviation of the FR method from CR is of the same order of magnitude as the uncertainty of CR of 10%, the deviation of the FR solution with respect to the CR solution is shown in Fig. 6. The deviation d is defined as:

$$d = \frac{St_{FR}}{St_{CR}} - 1.$$

(26)

The asymptote at approximately $x = 0.45m$ in the deviation plot appears where the Stanton number reaches zero. The asymptote in the Stanton number plot disappears in the deviation plot since the factor that adimensionalises the FR and CR Stanton number (the denominator in equation 25) is the same.

In order to get an averaged estimate of the deviation, the Root Mean Square (RMS) of the deviation is computed as follows starting from $x = 0.1m$ to avoid the influence of the leading edge discontinuity:

$$RMS_d = \sqrt{\frac{1}{L} \int_{0.1}^{L} d^2 dx}.$$

(27)

For P3 the two flux points closest to the asymptote are not taken into account in order to avoid the influence of the large deviation where $St = 0$, which does not indicate a large error. The values of RMS_d for P0 up to P3 are given in Table 2. As expected, the RMS deviation decreases with the polynomial order. Furthermore, the RMS deviation for P3 is close to the expected accuracy of 10% of the CR method. An RMS deviation of 0.1458 was obtained with DLR tau in [16], using the same definition of RMS_d as in Eq. 27 and not taking into account the deviation around the asymptote.
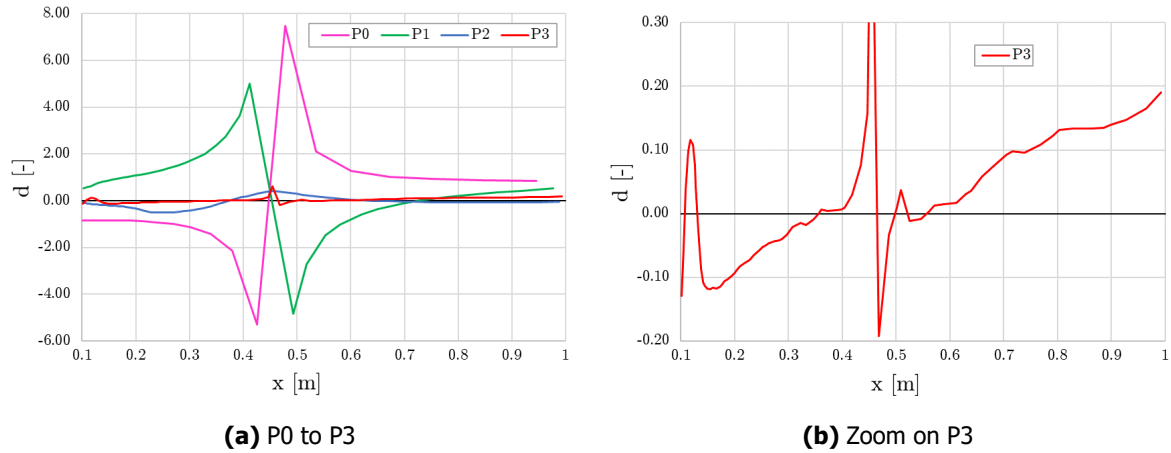
(a) P0 to P3   **(b)** Zoom on P3

Fig 6. Stanton number deviation

Table 2. RMS deviation of the Stanton number for different orders

| Order	P0	P1	P2	P3
RMS_d	2.327	1.252	0.2893	0.1105

4.2. Hypersonic Viscous Flow over a Cylinder

The second considered test case consists of a hypersonic viscous flow over a cylinder, which is widely used in the literature and was first proposed by Gnoffo in [21]. The considered geometry consists of a cylinder with radius 1m. The free stream values imposed are presented in Table 3.

Table 3. Free stream values for the hypersonic cylinder case

M_∞	p_∞ $[Pa]$	T_∞ $[K]$
17.605	57.602	200

The used mesh is presented in Fig. 7. The mesh consists of curved quadrilateral elements of second order and contains 297 elements: 11 in the circumferential direction and 27 in the direction normal to the cylinder. The inlet boundary is imposed as a Dirichlet boundary condition that sets the states to the free stream values. For the outlet, a supersonic outlet boundary condition is used. The cylinder is represented by an iso-thermal no-slip wall at a temperature T_w of 500K.
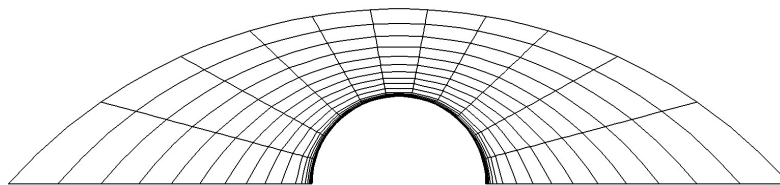
Fig 7. Mesh with 297 curved quadrilateral elements used for the hypersonic cylinder case

The FR method is used with a c_{SD} VCJH scheme [10] for the correction functions. The distribution of both the solution and flux points is the Gauss-Legendre distribution. For the convective interface fluxes, the AUSM$^+$ scheme is used, as proposed in [18, 19]. For the diffusive and artificial interface fluxes, the Local Approach scheme is used [20, 23]. For the LLAV scheme, κ is set to 0.5.

The pressure coefficient fields for a second-order and fourth-order of accuracy FR method are presented in respectively Fig. 8 and 9. Here the pressure coefficient is computed as follows:

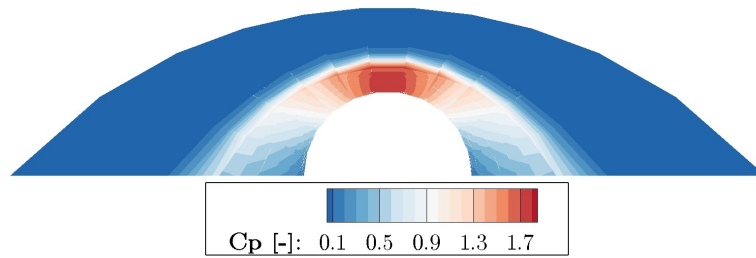$$Cp = \frac{p - p_\infty}{0.5\rho_\infty V_\infty^2}.$$

(28)
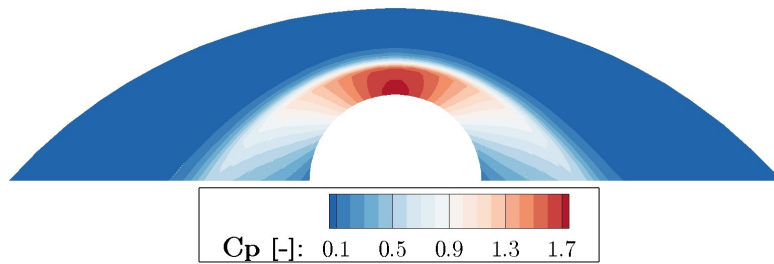

Fig 8. Pressure coefficient field for P1

Fig 9. Pressure coefficient field for P3

Fig. 10 and 11 show the artificial viscosity for the two cases. It is clear that the LLAV method is only active in the shock area. Fig. 12 shows the Stanton number as a function of θ of the first- to seventh-order of accuracy solutions, i.e. P0 to P6, compared to the one found in [1]. The variable θ is the angle along the cylinder, reaching $\theta = 0°$ in the stagnation point and $\theta = \pm90°$ in the two end-points of the considered half-cylinder. For P0 to P3 the heat flux is over-estimated, while for higher orders it coincides with the reference heat flux. A stagnation Stanton number of approximately 0.0082 is found, coinciding with the value found in [1, 22].
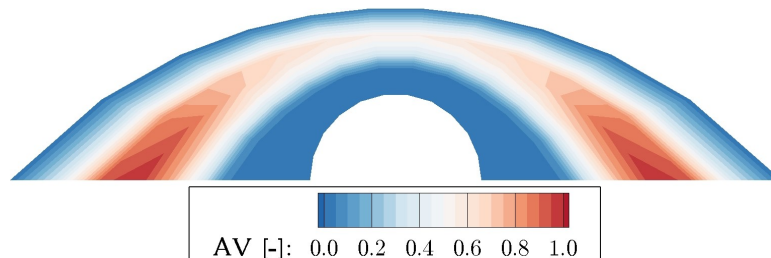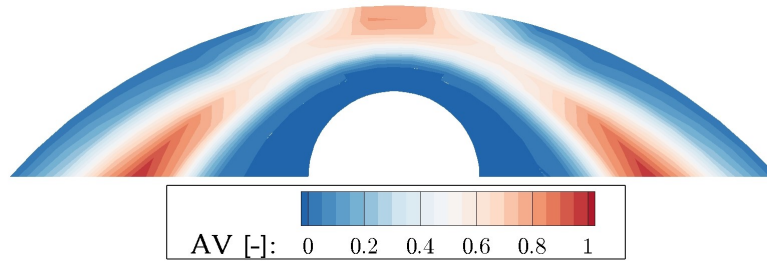

Fig 10. Artificial viscosity field for P1

The present test case is also executed on a coarser mesh, in order to obtain a tenth-order of accuracy solution (P9). The mesh is presented in Fig. 13 and contains 77 curved quadrilateral elements. The pressure coefficient field for the tenth-order of accuracy solution is presented in Fig. 14. The pressure coefficient on the stagnation line for the present case and the P1 and P3 solutions on the 297 element mesh as shown previously in figures 8 and 9, is shown in figure 15. Cp is plotted as a function of the

Fig 11. Artificial viscosity field for P3

| (a) Full simulated cylinder | (b) Zoom around stagnation point |
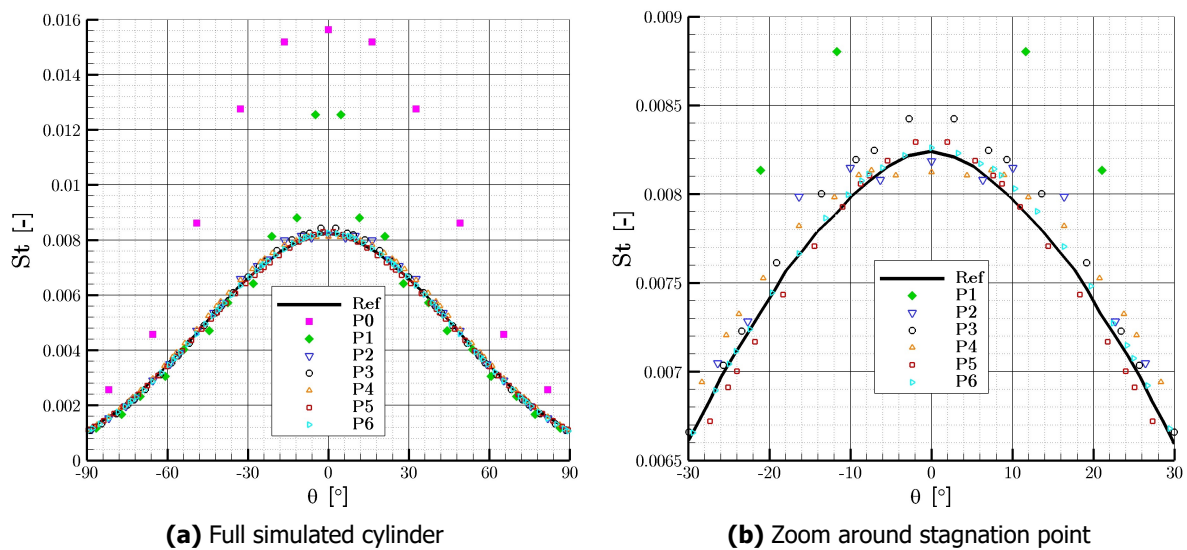
Fig 12. Stanton number for the hypersonic cylinder case

distance d to the cylinder normalized by the cylinder diameter D. As such, $d/D = 0$ corresponds to the stagnation point on the cylinder, while the inlet is positioned at $d/D = 0.5$. It is clear that for the P9 solution, the shock is resolved smoothly and no significant oscillations are present around the shock. For P3, there generally are no oscillations present, however, a slight discontinuity can still be seen on the downstream side of the shock, around $d/D = 0.14$. For P1 however, some over- and undershoots are observed due to the inaccuracy of P1 on the considered very coarse mesh.
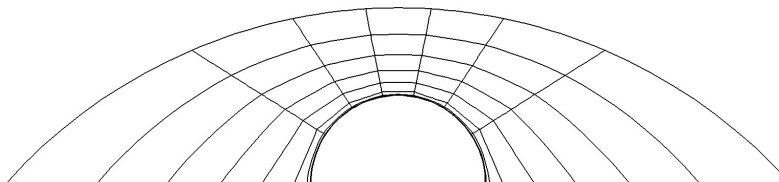

Fig 13. Coarse mesh with 77 curved quadrilateral elements for the hypersonic cylinder case

Fig. 17 shows the Stanton number for 3 cases with approximately the same amount of Degrees of Freedom (DoF): the present P9 case with 77 elements (7700 DoF), the P4 case presented previously with 297 elements (7425 DoF) and a P1 case on a mesh with 1891 elements (7564 DoF), of which Fig. 16 presents the mesh. All meshes have the same smallest element height of 1e-5m. Despite having approximately the same amount of degrees of freedom, it is clear that P4 and P9 significantly outperform

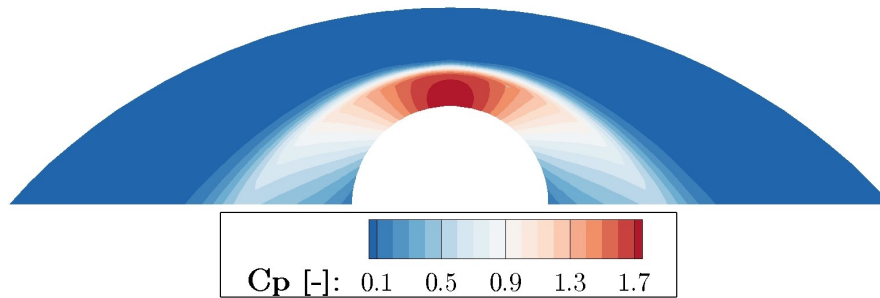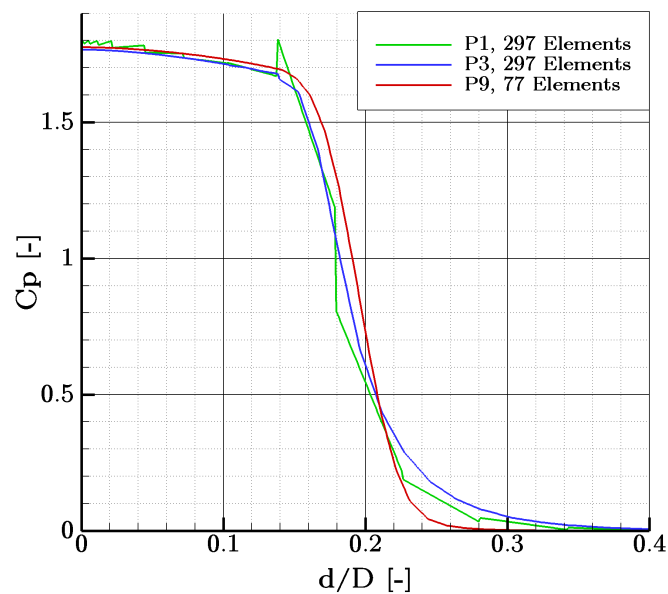**Fig 14.** Pressure coefficient field for P9

Fig 15. Pressure coefficient on the stagnation line as a function of the normalized distance to the cylinder for the P1 and P3 cases on the 297 element mesh and the P9 case on the 77 element mesh

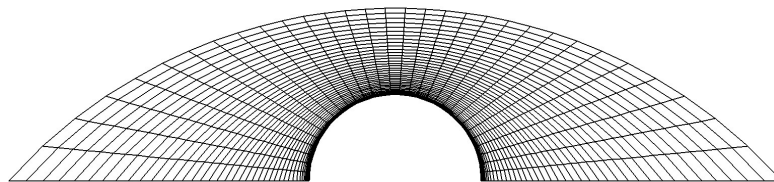P1 and have a much better agreement with the reference Stanton number.

Fig 16. Mesh with 1891 curved quadrilateral elements for the hypersonic cylinder case

Finally, in order to assess the influence of the different FR parameters as well as the shock capturing scheme on the heat flux prediction, a P1 simulation was done on a finer mesh for different settings of the FR method. The mesh used contains 3150 elements and is shown in Fig. 18. The case was run for different settings of the LLAV shock capturing scheme. Fig. 19a presents the Stanton number for different settings of κ, c and S_0. The final line in the legend represents a simulation where the smoothness detector S was computed based on the density ρ instead of the pressure p. It is clear that the predicted Stanton number does not greatly depend on the settings of the LLAV scheme. Additionally, even using
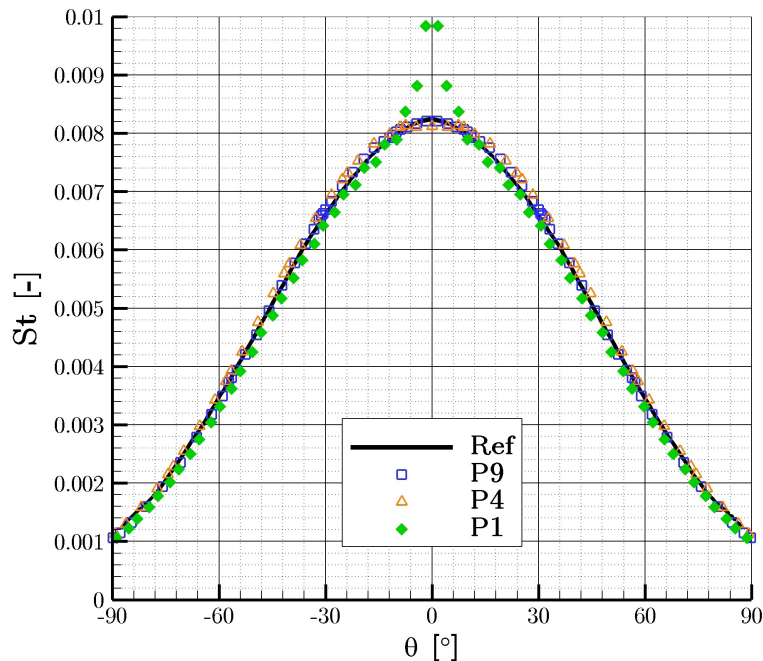
Fig 17. Stanton number for cases with approximately the same amount of DoF: P1, P4 and P9

density for the smoothness detector, a good heat flux is found, despite strong density gradients in the boundary layer, which can mistakenly be seen as a shock by the smoothness detector.

Fig. 19b presents the Stanton number prediction for the Gauss-Legendre and Gauss-Lobatto solution and flux point distributions and for an equidistant distribution. The influence on the Stanton number is again small, only the Gauss-Lobatto points under-perform in the stagnation point. This is consistent with the general lack of accuracy found when using Gauss-Lobatto points for FR [5].

Fig. 19c shows the Stanton number for different interface flux schemes. The convective schemes considered are: AUSM+, AUSM+Up [18, 19] and the Roe scheme [11]. The diffusive interface flux schemes considered are: Local Approach (LA) [20, 23] and the 2nd approach of Bassi-Rebay (BR2) [9]. Once again it is clear that the influence on the Stanton number is small.

Finally, Fig. 19d presents the Stanton number for different VCJH correction functions. The correction function for which FR reduces to Spectral Difference (SD), for which FR reduces to Discontinuous Galerkin (DG) [10] and the g2 correction function proposed by Huynh in [2] are considered. Also in this case, the predicted Stanton does not vary much with different forms of correction functions.
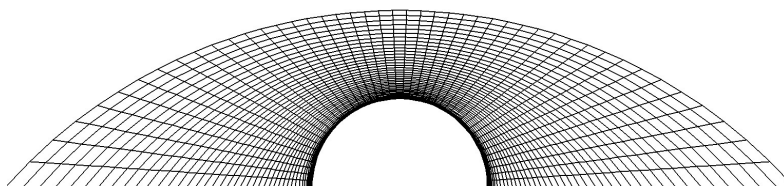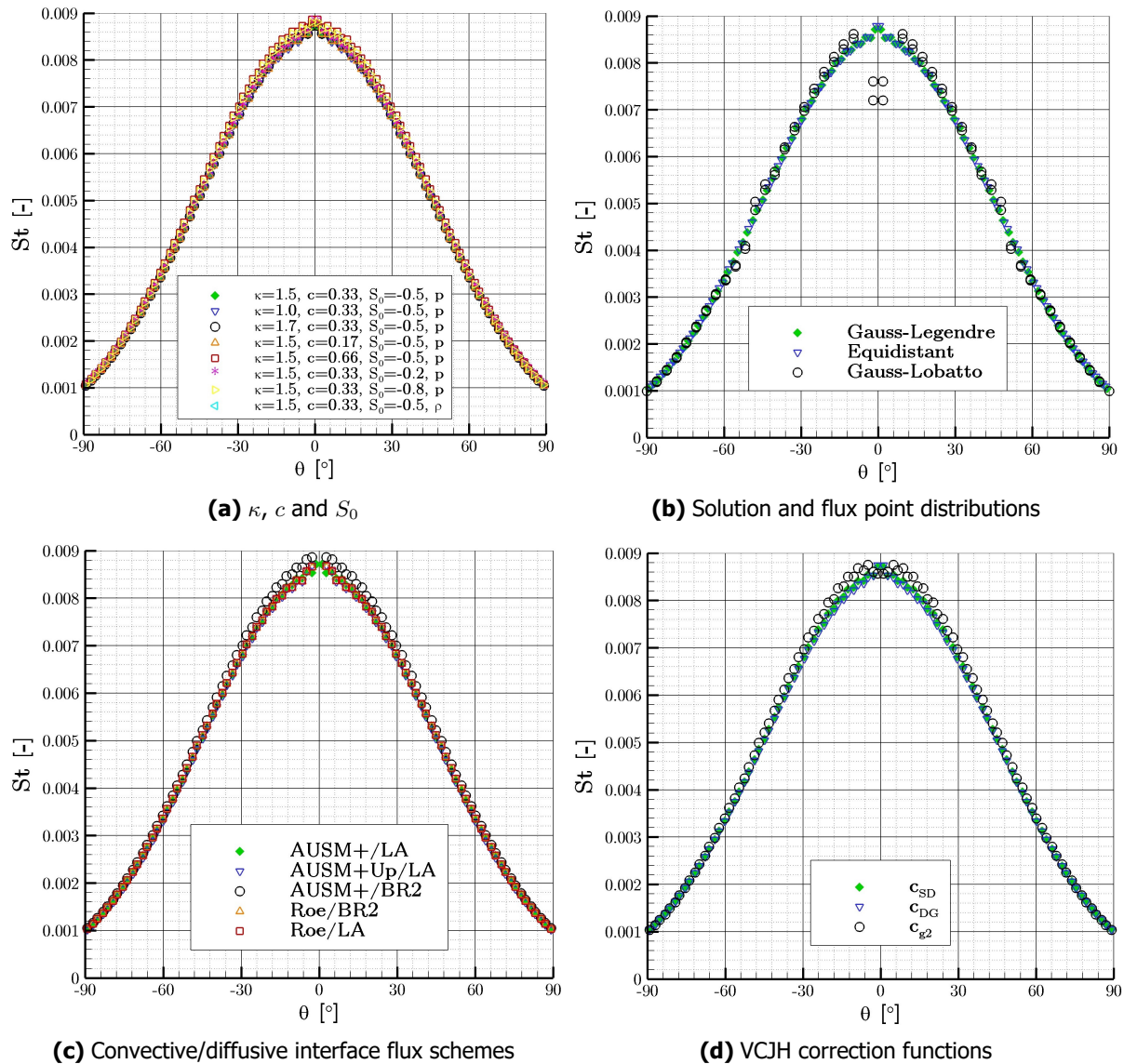

Fig 18. Mesh with 3150 curved quadrilateral elements used for the hypersonic cylinder test case

(a) κ, c and S_0

(b) Solution and flux point distributions

(c) Convective/diffusive interface flux schemes

(d) VCJH correction functions

Fig 19. Stanton number for different parameters

5. Conclusion

The developed FR and LLAV methods are successfully applied to two viscous high-speed benchmark test cases and are shown to obtain accurate heat flux predictions. For both cases relatively coarse meshes are used, where higher orders of accuracy, up to 10-th order, coincide closely with considered references. The predicted Stanton number is compared to both analytical results as well as numerical results from the literature. It is shown that for cases with a similar amount of DoFs, higher orders obtain more accurate heat flux predictions. Furthermore, the influence on the predicted heat flux of the parameters of the shock capturing method, as well as the characteristic parameters of the FR method, including the correction polynomials, the point distributions and the convective and diffusive interface flux schemes, was investigated. Only a minor influence was found for all investigated parameters.

6. Acknowledgements

References

[1] E. J. Ching, Y. Lv, P. Gnoffo, M. Barnhardt, and M. Ihme, "Shock capturing for discontinuous Galerkin methods with application to predicting heat transfer in hypersonic flows," *Journal of Computational Physics*, vol. 376, pp. 54–75, 2019.

[2] H. T. Huynh, "A flux reconstruction approach to high-order schemes including discontinuous Galerkin methods," *AIAA paper*, vol. 4079, p. 2007, 2007.

[3] H. T. Huynh, "A reconstruction approach to high-order schemes including discontinuous Galerkin for diffusion," *AIAA paper*, vol. 403, p. 2009, 2009.

[4] H. T. Huynh, "High-order methods including discontinuous Galerkin by reconstructions on triangular meshes," *AIAA Paper*, vol. 44, p. 2011, 2011.

[5] R. Vandenhoeck and A. Lani, "Implicit high-order flux reconstruction solver for high-speed compressible flows," *Computer Physics Communications*, 2019.

[6] R. Vandenhoeck, A. Lani, and J. Steelant, "Development of an implicit high-order flux reconstruction solver for the langtry-menter laminar-turbulent transition rans model," *Computer Physics Communications*, vol. 278, p. 108408, 2022.

[7] A. Lani, *An object oriented and high performance platform for aerothermodynamics simulation*. PhD thesis, Université Libre de Bruxelles, 2008.

[8] T. Quintino, *A component environment for high-performance scientific computing: design and implementation*. PhD thesis, KU Leuven, von Karman Institute for Fluid Dynamics, 2008.

[9] F. Bassi and S. Rebay, "A high-order accurate discontinuous finite element method for the numerical solution of the compressible Navier-Stokes equations," *Journal of computational physics*, vol. 131, no. 2, pp. 267–279, 1997.

[10] P. E. Vincent, P. Castonguay, and A. Jameson, "A new class of high-order energy stable flux reconstruction schemes," *Journal of Scientific Computing*, vol. 47, no. 1, pp. 50–72, 2011.

[11] P. L. Roe, "Approximate Riemann solvers, parameter vectors, and difference schemes," *Journal of computational physics*, vol. 43, no. 2, pp. 357–372, 1981.

[12] P.-O. Persson and J. Peraire, "Sub-cell shock capturing for discontinuous Galerkin methods," in *44th AIAA Aerospace Sciences Meeting and Exhibit*, p. 112, 2006.

[13] M. Yu, F. X. Giraldo, M. Peng, and Z. J. Wang, "Localized artificial viscosity stabilization of discontinuous Galerkin methods for nonhydrostatic mesoscale atmospheric modeling," *Monthly Weather Review*, vol. 143, no. 12, pp. 4823–4845, 2015.

[14] J. S. Park, T. K. Chang, and C. Kim, "Higher-order multi-dimensional limiting strategy for correction procedure via reconstruction," in *52nd Aerospace Sciences Meeting*, p. 0772, 2014.

[15] D. R. Chapman and M. W. Rubesin, "Temperature and velocity profiles in the compressible laminar boundary layer with arbitrary distribution of surface temperature," *Journal of the Aeronautical Sciences*, vol. 16, no. 9, pp. 547–565, 1949.

[16] H. Mandler, "Predictions of In-Flight Heating on a Hypersonic Vehicle," Master's thesis, Universität Stuttgart, Germany, 2019.

[17] J. D. Anderson Jr, *Hypersonic and high-temperature gas dynamics*. American Institute of Aeronautics and Astronautics, 2006.

[18] M.-S. Liou and C. J. Steffen, "A new flux splitting scheme," *Journal of Computational physics*, vol. 107, no. 1, pp. 23–39, 1993.

[19] M.-S. Liou, "On a new class of flux splitting," *Lecture Notes in Physics*, vol. 414, p. 115, 1993.

[20] K. Van den Abeele, "Development of high-order accurate schemes for unstructured grids," *Phd thesis in Vrije Universiteit Brussel*, 2009.

[21] P. Gnoffo and J. White, "Computational aerothermodynamic simulation issues on unstructured grids," in *37th AIAA Thermophysics Conference*, p. 2371, 2004.

[22] G. E. Barter and D. L. Darmofal, "Shock capturing with PDE-based artificial viscosity for DGFEM: Part I. Formulation," *Journal of Computational Physics*, vol. 229, no. 5, pp. 1810–1827, 2010.

[23] K. Van den Abeele, M. Parsani, and C. Lacor, "An implicit spectral difference Navier-Stokes solver for unstructured hexahedral grids," in *47th AIAA Aerospace Sciences Meeting including The New Horizons Forum and Aerospace Exposition*, p. 181, 2009.